Electrochimica Acta 542 (2025) 147515

Contents lists available at ScienceDirect

Electrochimica Acta

journal homepage: www.journals.elsevier.com/electrochimica-acta

Enhancing the supercapacitive properties of SnO_2 through W^{5+}/W^{6+} redox pairs☆

Karlo Maskaric [a,b], Ana Varadi [a,c], Ameen Uddin Ammar [a], Adriana Popa [a], Dana Toloman [a], Sergiu Macavei [a], Lucian Barbu Tudoran [a], Cristian Leostean [a], Emre Erdem [d,a], Maria Stefan [a,*], Arpad Mihai Rostas [a,*]

[a] National Institute for Research and Development of Isotopic and Molecular Technologies, Donat 67-103, Cluj-Napoca, 400293, Romania
[b] Biomolecular Physics Department, Babes-Bolyai University, Kogalniceanu 1, Cluj-Napoca, 400347, Romania
[c] Doctoral School of Chemistry, Babes-Bolyai University, Cluj-Napoca, 400084, Romania
[d] Faculty of Engineering and Natural Sciences, Sabanci University, Tuzla, Istanbul, 34956, Turkey

ARTICLE INFO

Keywords:
Supercapacitor
EPR spectroscopy
SnO_2
Tungsten
Nanomaterials

ABSTRACT

This research underscores the promising potential of SnO_2-based materials in high-performance supercapacitor applications, with W^{5+} and W^{6+} ions serving as dopants. A range of characterization and testing was performed to examine SnO_2 as an electrode material, focusing on understanding the influence of W ions on its electrochemical properties. Techniques such as scanning and transmission electron microscopy, X-ray diffraction, Raman spectroscopy, and photoluminescence spectroscopy were employed to analyze the morphology and structure. Changes in defect structures due to W-doping and its oxidation state were detected via electron paramagnetic resonance and X-ray photoelectron spectroscopy, confirming the presence of W^{5+}/W^{6+} redox pairs. An exhaustive electrochemical examination of undoped and W-doped SnO_2 was performed, tested as electrodes in all-in-one symmetrical supercapacitor setups, with detailed performance assessments following. Results indicated that W addition significantly enhanced the specific capacitance of the host material, achieving a specific capacitance of 268 F/g at a 0.5% W ion concentration, along with improved energy and power densities of 36.8 Wh/kg and 2650 W/kg, respectively. This enhancement is attributed to the variable valence states of W ions, with the mixed W^{5+}/W^{6+} state enhancing faradaic reactions and facilitating rapid charge transfer through hopping processes between different cation valence states at relatively low activation energies. Dunn's analysis of the best-performing supercapacitor device indicated that, at higher scan rates, capacitive processes dominate the energy storage mechanism, with electric double-layer capacitance and rapid surface redox reactions playing a key role, while at lower scan rates, diffusion-based processes become more significant. This suggests that, at lower scan rates, electrolyte ions can penetrate deeper pores and interact with the W^{5+}/W^{6+} redox-active sites introduced into the SnO_2 host.

1. Introduction

The growing scarcity of fossil fuels, combined with the increasing energy demand and environmental concerns, has driven the need for alternative and sustainable energy sources [1]. Renewable energy technologies, such as solar, wind, hydroelectric, and geothermal energy, are promising solutions but face intermittency, limited storage capacity, geographical constraints, and weather dependence [2]. To address these limitations, energy storage devices have become essential for stabilizing energy systems and ensuring reliability [3].

Batteries and capacitors are the most common energy storage technologies. Batteries offer a high energy density but are hindered by short lifetimes and low power density. Conversely, capacitors excel in recyclability and power density but suffer from low energy density [4]. Supercapacitors (SCs) have emerged as a hybrid solution combining both advantages. They offer high power density, rapid charge–discharge cycles, substantial storage capacity, low resistance, environmental friendliness, and long lifespans [5,6]. The electrode materials are vital components of SCs, significantly impacting the electrochemical performance of these devices. Modifying the properties

☆ Supplementary information available.

* Corresponding authors.
E-mail addresses: maria.stefan@itim-cj.ro (M. Stefan), arpad.rostas@itim-cj.ro (A.M. Rostas).

https://doi.org/10.1016/j.electacta.2025.147515
Received 12 August 2025; Received in revised form 19 September 2025; Accepted 26 September 2025
Available online 10 October 2025

of the electrode material could help increase the specific capacitance of SCs, expanding the device's energy density as well [7]. The specific capacitance (C_P) and energy density (E_D) are directly proportional, as described by $E_D = C_P \cdot \Delta V^2$, ΔV^2 being the operating voltage window. Therefore, the optimal electrode material must have a high surface area, controllable and increased porosity, high thermal and chemical stability, many electrochemical sites, and a defective structure [8,9].

Metal oxides (MO) offer pseudocapacitance and other properties for cost-effective electrode material, such as large surface area, good reproducibility, high defect structure, nontoxicity, low cost, and abundance in the environment [10,11]. The commonly used metal oxides are nickel oxide (NiO), ruthenium dioxide (RuO_2), manganese oxide (MnO_2), and iridium oxide (IrO_2), which have been used as electrode material in SCs, with literature demonstrating their good performance. Tin oxide (SnO_2) is an n-type semiconductor with a wide band gap of 3.62 eV, high electron mobility of 100–200 cm^2/V, excellent long-term stability, rapid electron transport, and it offers pseudocapacitance. At the same time, it is a structurally stable material that is also cheap and abundant, making it a cost-effective electrode material [12]. The surface and the interior of SnO_2 electron transport layer can contain a substantial number of Sn interstitial defects (Sn_i) and oxygen vacancy defects (V_O).

Although the electrochemical performance of MOs shows promising values, it can be further enhanced through various techniques. One of the most effective ways to enhance the performance of MOs is by doping, which alters their structure and improves the photocatalytic and electrochemical properties of the active electrode material. Though reports are scarce, Tungsten (W) doped MOs have previously been reported as electrode materials for SC applications. Ahmed et al. [13] demonstrated pseudocapacitance in nano-sheets of W-doped NiO fabricated by a facile hydrothermal treatment. Besides the nano-sheet morphology, W doping significantly influenced the electrochemical performance. Due to a higher surface-to-volume ratio, the maximum specific capacitance of 872.32 F/g in 4 percent W-doped NiO is greater than in several other NiO-based materials. Their nanosheets showed high charging-discharging retention (84.38%) and reasonable cyclic stability (87.5%) after 3000 CV cycles at a 5 mV/s scan rate.

Huo et al. [14] have found that the electrical conductivity of SnO_2 doped with Mo or W can be increased by one order. Thus, there is a possibility to modify the electrochemical properties of SnO_2 by different doping strategies [15]. Gao et al. [16] synthesized SO_4^{2-}/SnO_2 by precipitation and calcination. Their SO_4^{2-}/SnO_2 electrode exhibited a specific capacitance of 51.95 F/g, demonstrating good stability over more than 2000 cycles at a scan rate of 5 mV/s. Varshney et al. [17] synthesized mesoporous SnO_2-NiO nanocomposites using modified sol gel method. The SnO_2-NiO nanocomposite electrode exhibited capacitive behavior, with a maximum specific capacitance of 464.67 F/g at a scan rate of 5 mV/s. Nithiyanantham et al. [18] synthesized chain-like SnO2 nano-assemblies at room temperature by a simple wet chemical route within an hour, using DNA as a scaffold. Various specific capacitance values were obtained, depending on the morphology of the resulting nanostructures, with the highest value being 209 F/g at a scan rate of 5 mV/s, retaining approximately 71% of the initial specific capacitance after 5000 cycles.

These previous studies highlight the potential of SnO_2 based materials for high-performance supercapacitor applications. In the present study, SnO_2 was doped with 0.5% tungsten (W), and the undoped and doped materials were thoroughly characterized and tested as electrode material to understand how W doping affects the electrochemical performance of SnO_2. Morphological and structural characterization was achieved using scanning and transmission electron microscopy (SEM/TEM), X-ray diffraction (XRD), and X-ray photoelectron spectroscopy (XPS). Alterations in the defect structure due to the introduction of the dopant were observed from analysis of the electron paramagnetic resonance (EPR) and the photoluminescence (PL) spectroscopy. Finally, each sample underwent comprehensive electrochemical measurements by making all-in-one symmetrical (SC) devices, followed by a detailed performance evaluation.

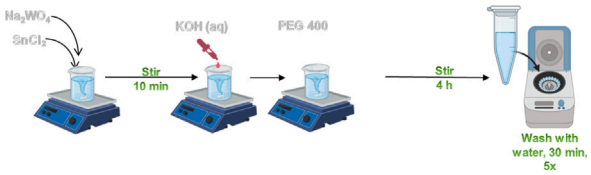

Fig. 1. Schematic representation of the synthesis steps for the undoped and W-doped SnO_2 samples.

2. Materials and methods

2.1. Materials and synthesis

Undoped and W-doped (0.1, 0.3, 0.5, and 0.7%) SnO_2 samples were synthesized to demonstrate how the dopant affects the electrochemical and structural characteristics of SnO_2 nanoparticles. A maximum of 0.7% W dopant concentration was chosen to prevent the formation of secondary WO_3 phases and to ensure good dispersion of the W ions in the host material, thereby avoiding dipolar interactions between the paramagnetic ions and resulting in a better-resolved EPR spectrum. The samples were labeled SnO_2:W(x), with x = 0, 0.1, 0.3, 0.5, and 0.7%.

The W-doped SnO_2 nanoparticles were synthesized following a chemical precipitation method, reported in earlier works, with some minor modification [19,20], following the reaction scheme presented in Fig. 1. Firstly, 100 ml of aqueous solution containing 0.4 g of $SnCl_2 \cdot 2H_2O$ and x% of sodium tungstate was precipitated using 100 ml of KOH solution (3.1 mM) until the pH value reached 11. The chemical reaction was then continued by adding 3 mL of polyethylene glycol 400 (PEG400) and stirring for 3 h (aging time). Centrifugation was employed to separate the precipitate, cleaned 5 times with double-distilled water before being dried in an oven at 70 °C for 12 h. The undoped and W-doped SnO_2 nanoparticles were annealed at 550 °C for 2 h before being characterized. All used chemicals were of analytic quality and were used as such without further purification.

2.2. Characterization methods

A Hitachi HD-2700 microscope was used to assess the morphology of undoped and W-doped SnO_2 samples by scanning transmission electron microscopy (STEM). A Smart Lab Rigaku diffractometer with Cu–Kα radiation was used to measure X-ray diffraction (XRD). All measurements were performed in the 10 to 90° range, with a 0.01° step. X-ray photoelectron spectroscopy (XPS) was used to investigate the sample surface composition using a custom-built SPECS spectrometer equipped with a monochromatic Al anode (1486.71 eV). The XPS spectra were analyzed using the CasaXPS software. Integral intensities were calibrated with the corresponding relative sensitivity, transmission, and electronic mean free path factors from the CasaXPS database. The spectra were calibrated concerning the 284.6 eV adventitious C1s core-level line. A Shirley background was extracted from the spectra. An FS5 spectrofluorometer (Edinburgh Instruments), equipped with a 150 W CW Ozone-free Xenon arc lamp, a Czerny–Turner with plane grating monochromators, and a PMT-900 emission detector, was used to collect photoluminescence spectra (PL). Electron paramagnetic resonance (EPR) spectroscopy was performed at room temperature using a dual-band Bruker E-500 ELEXSYS spectrometer operating at an X-band frequency of 9.88 GHz. Measurements were performed under identical conditions with equal sample quantities to ensure consistency.

2.3. Supercapacitive properties measurements

Symmetrical all-in-one supercapacitor devices were assembled using undoped and W-doped SnO_2 in 200 μL of 6 M KOH as electrolyte separated by a glass fiber separator, as presented in Fig. 2. The choice

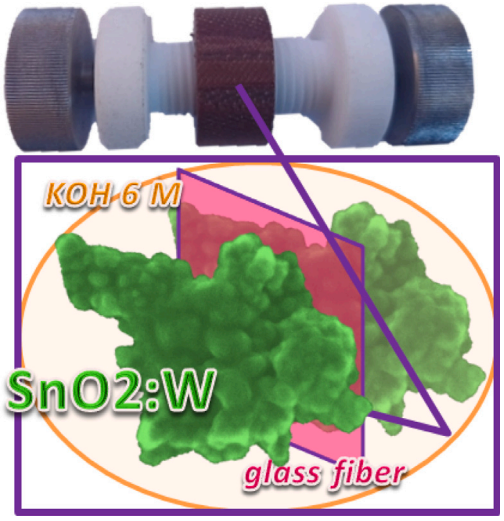

Fig. 2. Schematic representation of the 2-electrode symmetric supercapacitor devices used in this study.

of 6 M KOH as the electrolyte is based on its well-established use in supercapacitor systems, particularly for metal oxide-based electrodes such as SnO_2. KOH offers high ionic conductivity, chemical stability, and rapid ion transport, essential for evaluating the intrinsic electrochemical behavior of the electrode materials. A higher concentration, such as 6 M, ensures sufficient OH^- ions to support fast and reversible charge storage mechanisms, including electric double-layer and surface Faradaic reactions. The supercapacitor consisted of two circular-shaped bolts as current collectors. The areal mass loading of the electrodes on this device is approximately 2.65 mg/cm^2, with a total mass of 3 mg per electrode. A BioLogic VMP 300 electrochemical workstation was used to test the electrochemical performance of the electrode materials. The techniques included cyclic voltammetry (CV), potentiostatic electrochemical impedance spectroscopy (PEIS), and galvanostatic cycling with potential limitation (GCPL). CV measurements were performed within a voltage window of 0 to 1 V, with scan rates ranging from 2 to 200 mV/s. PEIS was performed with an AC signal amplitude of 10 mV across a frequency range of 10 mHz to 1 MHz. GCPL tests were conducted at a current density of 0.8 A/g. Specific capacitance, energy density, and power density were calculated based on data from CV and GCPL.

3. Results and discussion

Before being used in SC applications, the undoped and W-doped SnO_2 samples were thoroughly morphostructurally characterized using various techniques, including scanning electron microscopy (SEM)/transmission electron microscopy (TEM), energy-dispersive spectroscopy (EDS), X-ray diffraction (XRD), ultraviolet–visible spectroscopy (UV–Vis), and Raman spectroscopy.

The SEM and TEM images corresponding to the SnO_2:W 0 and 0.5% samples are shown in Figure S-STEM⋆, 3a and b, indicating the formation of polyhedral nanoparticles with an average size of 15 nm, while the elemental distribution, obtained using EDS mapping (Fig. 3c), confirms a uniform distribution of the Sn and O atoms and the doping W ions in the SnO_2 nanoparticles, demonstrating that the doping process was successful and that the W ions are present in the samples. The doping W ions do not change the shape and size of the host SnO_2 material.

XRD was performed further to evaluate the effect of the dopant W ions on the SnO_2 structure. Fig. 3d shows the obtained diffractograms, where it can be seen that all the diffraction peaks could be identified as being part of a rutile-type structure with tetragonal symmetry (00-021-1250) specific for SnO_2. Rietveld analysis of the diffractograms allowed the determination of the lattice parameters and the unit cell volume. The results are presented in Table 1, where doping increases the unit cell volume slightly. This increase was not expected since the ionic radius of the W ions in different oxidation states is lower than that of Sn^+ (0.67 Å) [21]. The increase of the unit cell can be due to the appearance of oxygen vacancies by replacing Sn^{4+} ions with W^{6+} ions, which is the most stable oxidation state of tungsten [21,22]. The Sn vacancies could compensate for the extra positive charge in the crystal lattice of SnO_2 by doping with a higher oxidation state ion. The crystallite size (d) remains relatively unchanged by doping, indicating that the presence of W ions in the host lattice does not significantly impact the growth of the crystallites.

Table 1
Lattice parameters, unit cell volume, crystallite size, and band gap energy of the undoped and W-doped SnO_2 nanoparticles.

Sample	$a = b$ /Å	c /Å	V /Å^3	d /nm
SnO_2	4.7349(15)	3.1847(19)	71.4	10.4
SnO_2:W 0.1%	4.7385(13)	3.1846(14)	71.5	9.3
SnO_2:W 0.3%	4.7346(11)	3.1851(13)	71.4	11.5
SnO_2:W 0.5%	4.7351(14)	3.1853(15)	71.42	10
SnO_2:W 0.7%	4.736(2)	3.185(2)	71.43	10

The Raman spectra of the undoped SnO_2 showed typical peaks for tetragonal rutile structure at 467, 621, and 764 cm^{-1}, corresponding to the E_{1g}, A_{1g} and B_{2g} vibration modes, respectively. The peaks of the same vibrational modes for W doped SnO_2 experienced shifts as depicted in Fig. 3e; 469 and 616 corresponding to E_{1g} and A_{1g}. Additionally, two new peaks appeared in the doped SnO_2 at 238 and 275 cm^{-1}, attributed to different types of oxygen vacancies. Liu et al. [23] concluded that the IR active mode ~234 cm^{-1} can transform into Raman active mode due to the relaxation of the k = 0 rule, induced by subbridging oxygen vacancies.

The surface composition of the SnO_2:W 0.7% sample was analyzed with XPS. In Figure S-XPS⋆, the survey spectrum is represented, where the elements Sn, W, O, and C were successfully identified. For the quantitative analysis of the samples, the spectral lines corresponding to Sn3*d*, O1*s*, W4*f*, and C1*s* were recorded. Fig. 4a presents the deconvolution of the Sn3*d* spectrum. Sn $3d_{5/2}$ positioned at 486.8 eV and $3d_{3/2}$ positioned at 495.2 eV are characteristic of the Sn^{4+} oxidation state [21,24]. Also, two shake-up satellites were used in the deconvolution process, which can be observed at higher binding energies. Fig. 4b shows the deconvolution of the W4f spectrum, considering a small stoichiometric variation corresponding to oxygen vacancies. This is expected at the nanoscale and also confirmed by Raman measurements. W $4f_{7/2}$ positioned at 35.7 eV and $4f_{5/2}$ at 37.9 eV is characteristic of the W^{6+} oxidation state as also observed in SnO_2:W doped with higher 4 and 5% concentrations [21,24]. The W^{5+} oxidation state is observed at lower binding energies, $4f_{7/2}$ positioned at 34.8 eV and $4f_{5/2}$ at 37.0 eV [25]. The calculated W^{5+}/W^{6+} ratio is 0.24. The W doping was calculated from the integral intensities of the XPS core-level peaks, with a W:Sn atomic ratio of 0.0045, indicating that the doping process was successful and that the desired dopant ion concentration is present in the sample.

PL spectroscopy was performed on the SnO_2-based samples to get information on the defect-related emissions. An excitation wavelength of 325 nm was used, and the results are shown in Fig. 5a. Both undoped and W-doped SnO_2 show one high-intensity peak centered around 420 nm. The high-intensity peak of PL is associated with surface defects such as oxygen vacancies (V_O), which are widely reported for SnO_2 [26,27]. However, some sources suggest that the emission is due to Sn vacancies (V_{Sn}), which provide acceptor levels below the conduction band edge [28]. Some weaker emission peaks appear around 438

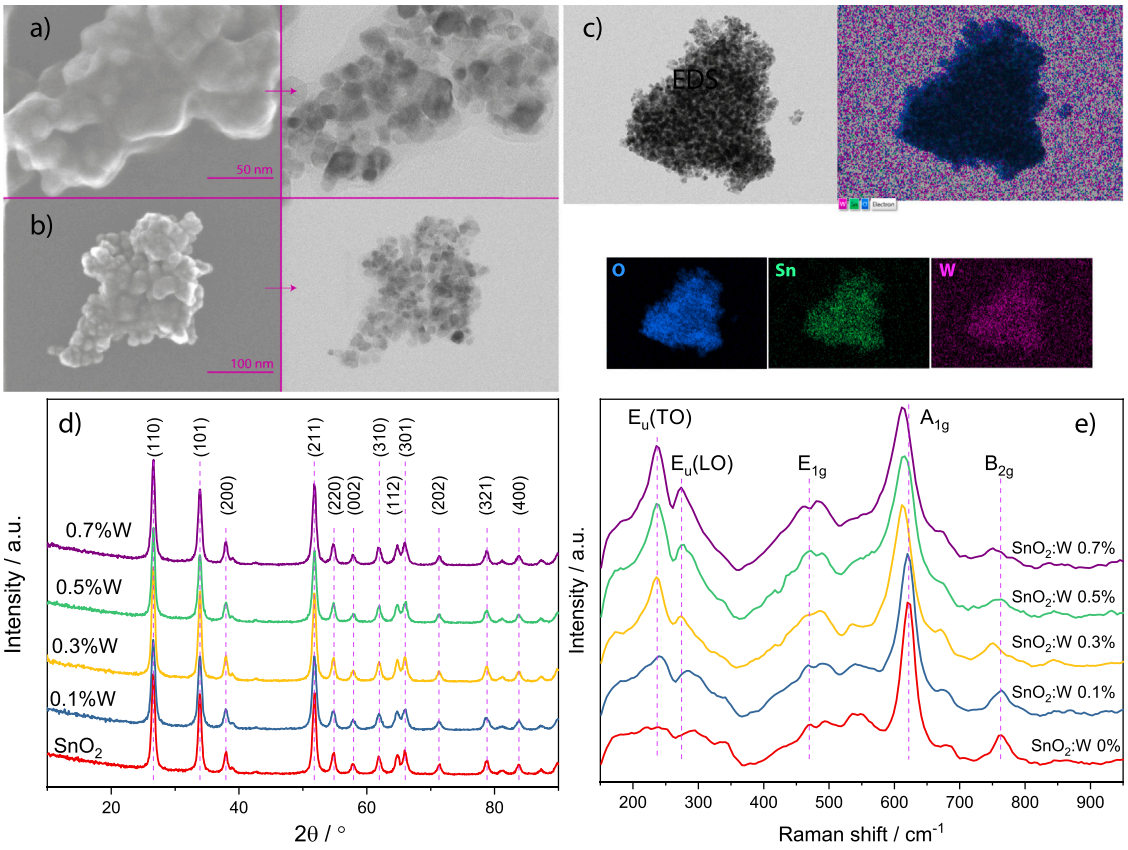

Fig. 3. SEM (a) and TEM (b) micrographs of the SnO_2:W 0.7% sample showing the nanostructure of the material. Elemental analysis performed by EDS (c). XRD diffractograms (d) and Raman spectra of the undoped and W-doped SnO_2 samples.

and 451 nm. These emissions are associated with other defect centers, such as Sn interstitials or dangling bonds of the nanocrystal [27]. The reduction in the intensity of this peak for the W-doped samples, except for 0.3%, shows that the doping ions are replacing the intrinsic vacancies and suppressing the defect-related emissions. Fig. 5b and S-PL* show the Gaussian deconvolutions of the PL spectra of the undoped and W-doped samples. The deconvolutions show the reduction of the total blue emission area of the W-doped samples compared to the undoped SnO_2, which shows that defect-related emission is reduced by introducing W ions.

The undoped and W-doped SnO_2 samples were analyzed using electron paramagnetic resonance (EPR) spectroscopy, a powerful tool for detecting and characterizing paramagnetic centers present in materials. In SnO_2, defects such as reduced tin cations and singly ionized oxygen vacancies can be present, which are EPR active. The EPR spectra are presented in Fig. 5c, where the undoped SnO_2 has one low-intensity resonance line with a g-value of 1.9, which is too small to be attributed to oxygen vacancies. Hajimoto et al. [29] identified this signal in similar SnO_2 samples and attributed it to interstitial Sn^{3+} defects, while Itoh et al. [30] attributes it to Sn^{3+} paramagnetic centers on the surface of reduced SnO_2-based materials. Silva et al. [31] observed two isotropic EPR signals with g = 2.014 and $g = 1.994$ and attributed them to Sn^{3+} centers in $SrSnO_3$ perovskites. Thus, we attribute the EPR signal with $g = 1.9$ observed for the undoped SnO_2 sample to reduced Sn^{3+} centers in SnO_2.

The Sn^{3+} related EPR signal disappears once the W-dopant is added to the system, indicating that tungsten replaces these centers in good accordance with the PL results. At the same time, a strongly distorted rhombic EPR signal at higher magnetic fields (350–420 mT region) is observable with g ~ 1.7, which we associate based on literature to W^{5+} (d1) ions in distorted environments [32–34].

The electrochemical performance of the synthesized samples was tested by assembling an all-in-one symmetric two-electrode system supercapacitor device. 6 M KOH was used as the electrolyte, with glass fiber as the separator.

CV characterization was performed to obtain information on the reaction kinetics and the type of charge storage phenomenon that dominated the reaction. Fig. 6a shows the CV curves of the undoped and W-doped SnO_2-based supercapacitor devices, measured at 100 mV/s in the 0–1 V voltage window. The CV curves of the devices exhibit a significant difference in shape as the W-dopant concentration increases, highlighting the impact of the doping ions on the device's electrochemical performance. The undoped SnO_2 shows a non-ideal quasi-rectangular CV curve, which illustrates a deviation from an ideal EDLC-type supercapacitor CV curve, that shows a perfect rectangle shape [35,36]. The rounding of the edges in practical supercapacitor devices, due to internal resistance between the components and the influence of faradaic reactions, leads to a sharp increase in the current value at maximum voltage, facilitating this shift from ideal rectangular behavior [35]. Transition metal oxides are generally associated with a pseudo-capacitance behavior in supercapacitor devices as the transition metals have variable oxidation states, favoring faradaic reaction at the electrode-electrolyte surface [9]. The undoped SnO_2 based device shows the lowest current value along with the smallest area of the curve compared to all other devices, indicating that even low W-dopant concentrations positively impact the SnO_2 electrochemical performance. Figure S-CV* shows the CV scans for all devices measured at different scan rates, which is important to analyze the rate capability, reversibility, and charge storage phenomenon evolution with changing scan rate. The multiple scan rate CV for undoped SnO_2 shows that the CV curve becomes more rectangular at lower scan rates, shifting towards ideal EDLC behavior as ions have enough time to access the full surface area. As the scan rate increases, the CV curves start to distort and skew

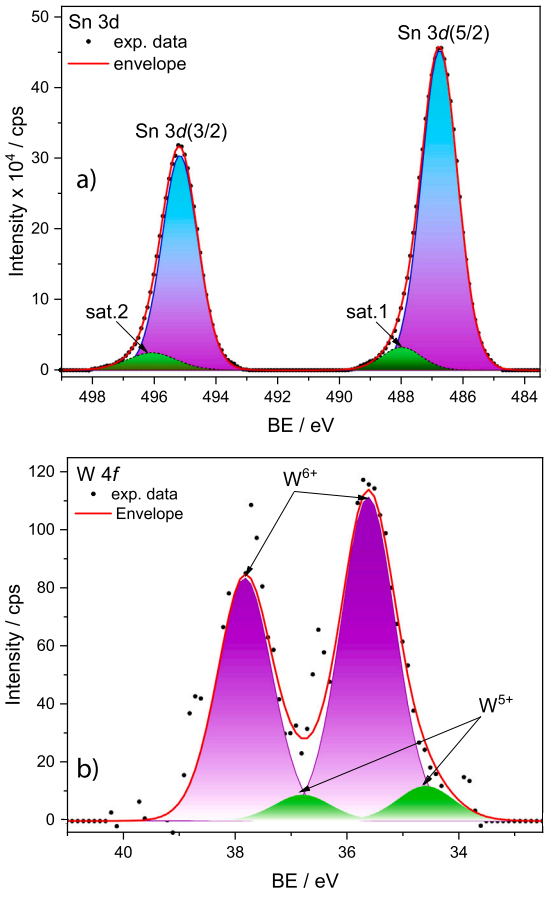

Fig. 4. Deconvoluted XPS spectra of Sn3d (a) and W4f (b) spectral lines measured on the SnO_2:W 0.7% sample.

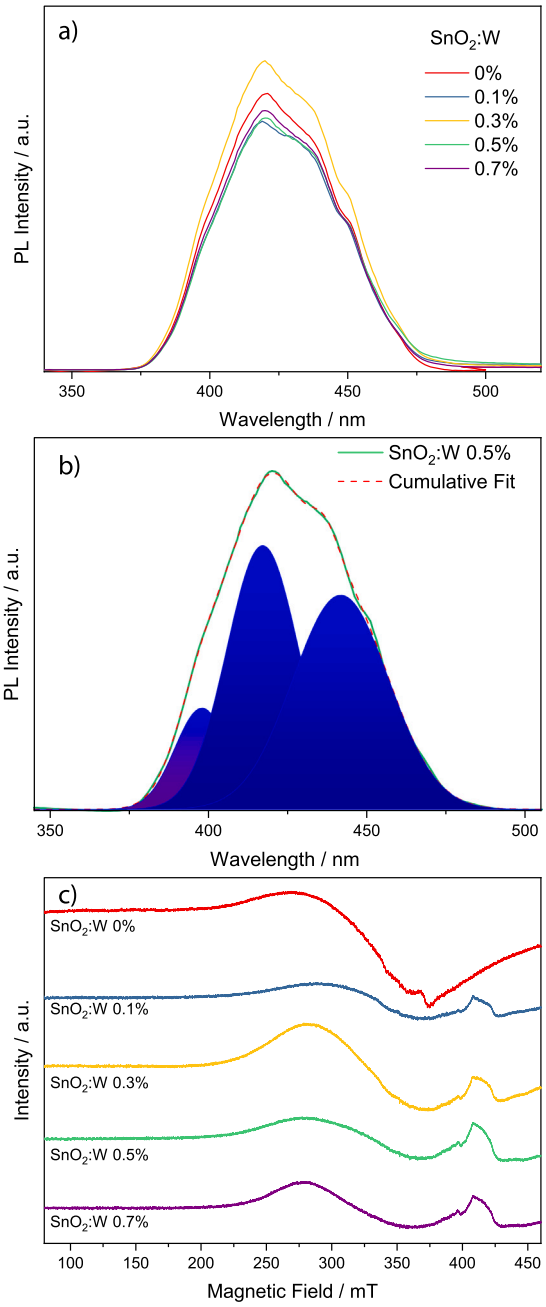

Fig. 5. Photoluminescence spectroscopy of undoped and 0.5% W-doped SnO_2 samples (a) and Gaussian fit of the PL spectra of 0.5% W-doped SnO_2 sample (b). EPR spectra of the undoped and 0.5% W-doped SnO_2 samples.

further from a rectangular shape, indicating the reduced accessibility of internal surface area and slower ion transport kinetics. The loss of ideal capacitive shape at high scan rates confirms that charge storage in the undoped SnO_2-based supercapacitor device is primarily governed by surface-limited EDLC processes, with no significant pseudocapacitive contribution and limited electronic conductivity.

Compared to the undoped SnO_2, which displays ideal EDLC behavior with nearly rectangular CV-shaped curves, the 0.1 and 0.3% W-doped SnO_2-based devices showed higher current values and increased pseudocapacitive behavior. The 0.1% W-doped sample exhibits a slight Faradic hump in its CV curves, particularly at lower scan rates, as can be seen in Fig. 6 and S-CV*, and far higher current response. This feature suggests the emergence of surface redox reactions, indicating that low-level W doping begins to introduce pseudocapacitive characteristics. Incorporating W^{5+} or W^{6+} ions likely generates oxygen vacancies and localized redox-active sites, enhancing the electrochemical reactivity of the electrode surface. At 0.3% W-doping, this pseudocapacitive contribution becomes more subtle in influence, with broader and more asymmetric CV shapes developing as the scan rate increases, with a lower current response than in the case of 0.1% W-doped based device, but a visible rise in the area of the CV curve. Despite the increased redox behavior, the curves retain a significant capacitive character, indicating a mixed mechanism involving both EDLC and Faradaic processes.

The CV curve of the SnO_2:W 0.5 and 0.7% -based supercapacitor devices show a complete shift from the ideal EDLC-type behavior and a dominant pseudo-capacitance type behavior along with prominent redox peaks and a significant increase in the current response, which signifies that the addition of W ions in SnO_2 leads to further diffusion of ions from the surface to the bulk of the material, improving the electrochemical properties of the device. Fig. 6 shows that SnO_2:W 0.5% based device reported the highest current response and the highest area of the CV curve.

The specific capacitance value can be calculated using the area under the CV curve using the following equation: $C_s = \frac{\int_{V_1}^{V_2} I(V)\mathrm{d}V}{2mK\Delta V}$, where C_s is the specific capacitance, $\int_{V_1}^{V_2} I(V)\mathrm{d}V$ represents the area under the CV curve, m is the mass of the active electrode material, K is the scan rate at which the CV was acquired and ΔV is the voltage window. The specific capacitance values obtained at different scan rates are presented in Fig. 6b. The SnO_2:W 0.5%-based device shows significantly higher specific capacitance values at each scan rate compared to the undoped SnO_2 and other W-doped SnO_2 devices. The highest

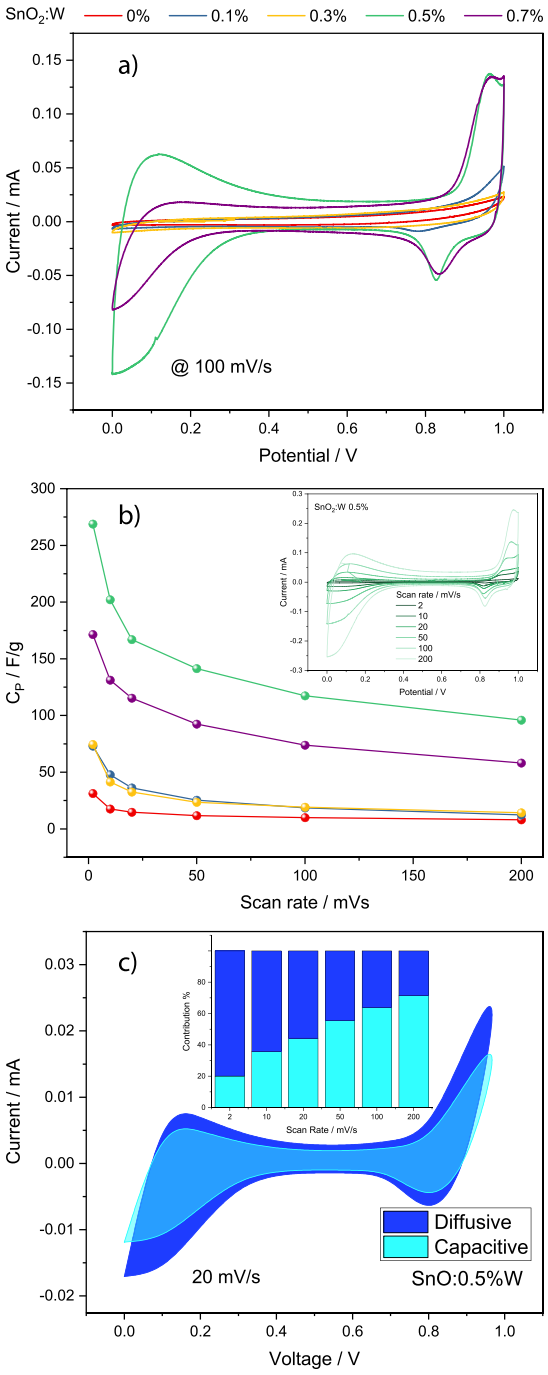

Fig. 6. Cyclic voltrammetry curves measured at 100 mV/s scan rate (a) and C_P values obtained at different scan rates for the undoped and 0.5% W-doped SnO_2 samples. Capacitive and diffusive contributions to the energy storage process obtained with the Dunn method for the W-doped SnO_2 sample (c).

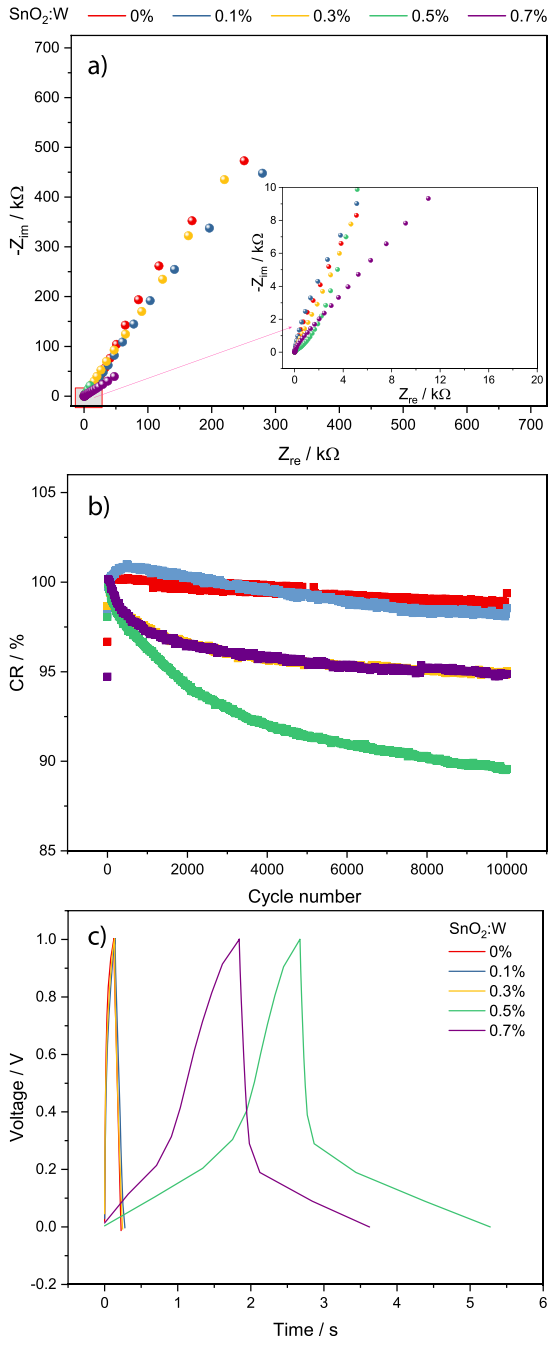

Fig. 7. Nyquist plots with the inset showing the high-frequency region (a), capacitance retention (b), and Galvanostatic Charge–discharge results of the supercapacitors employing undoped and W 0.5%-doped SnO_2 as electrode materials.

specific capacitance value recorded for SnO_2:W 0.5%-based device was 268 F/g at 2 mV/s followed by SnO_2:W 0.7% based device, which showed 172 F/g at 2 mV/s. The undoped SnO_2 based device shows the lowest specific capacitance value at each scan rate, highlighting the positive impact of W doping. The trend suggests that the increase in W doping concentration increases the supercapacitor performance up to a certain concentration, after which a saturation point is reached; further increases in dopant concentration decrease the supercapacitor performance. Table 2 shows the maximum specific capacitance value obtained from all the devices, with energy and power density values calculated from this specific capacitance value. Energy and power density values are standard performance metrics for energy storage devices. The best performing SnO_2:W 0.5% based devices showed the highest energy and power density, followed by SnO_2:W 0.7%, while the undoped device showed the lowest energy and power density values.

To observe the contribution of diffusive and capacitive phenomena in the energy storage process of the W-doped sample, a Dunn analysis for the best-performing SnO_2:W 0.5% based SC device was performed [37]. The equation used to calculate the contributions is expressed as $I(V) = k_1 \cdot \upsilon + k_2 \cdot \sqrt{\upsilon}$, where k_1 represents the capacitive current, k_2 represents the diffusive current, and υ is the scan rate.

Table 2
Equivalent circuit values obtained from Z-fitting of the Nyquist plots, and energy (E_D) and power (P_D) density values of the undoped and W-doped SnO_2.

Sample	R_1/Ω	$C_{dl}/\mu F$	R_2/Ω	C_{sp}/F/g @ 2 mV/s	E_D/Wh/kg	P_D/W/kg
SnO	2.48	2.76	496	31.27	4.34	312
SnO:W 0.1%	2.31	4.85	8612	73.12	10.15	730
SnO:W 0.3%	5.22	19.20	687	74.51	10.34	744
SnO:W 0.5%	1.19	8.39	350	268	36.8	2650
SnO:W 0.7%	1.53	1.37	64.76	171.48	23.82	1715

The relative contributions of each mechanism can be quantified by analyzing the slope and intercept of a Dunn plot. In the inset of Fig. 6c, the percentage contribution at different scan rates is presented; the capacitive contribution dominates at high scan rates, while the diffusion contribution starts to dominate at lower scan rates. It aligns with the CV curves observation, where we report that EDLC and pseudo-capacitance are involved in charge storage. The Dunn analysis suggests that at higher scan rates, charge storage is primarily governed by surface-controlled processes, such as electric double-layer capacitance and fast surface redox reactions, and as we move to lower scan rates, where the diffusion-controlled processes are more significant, indicating that electrolyte ions have sufficient time to access deeper pores and interact with redox-active sites. Fig. 6c shows the capacitive and diffusive contributions for the W 0.5%-doped SnO_2 sample at 20 mV/s, where almost 60% contribution comes from the diffusive part.

EIS spectroscopy is another powerful method to characterize the electrochemical performance of supercapacitor devices. It can provide valuable information on the resistance in the charge flow, which can be linked to the device's performance. Fig. 7a shows the Nyquist plot of all the supercapacitor devices using undoped and W-doped SnO_2 electrodes. Nyquist plots are a standard method to present EIS data, where imaginary impedance values are plotted against real impedance.

In line with the CV results, we observe that the SnO_2:W 0.5% and SnO_2:W 0.7% based supercapacitor devices have the smallest diameter of the Nyquist plot compared to the other devices, which show a significantly larger diameter, indicating a higher resistance to charge. The inset of Fig. 7a shows the enlarged area of the high-frequency region; the x-intercept in the high-frequency region shows the value of the solution resistance (R_s), which is the natural resistance between the electrode and electrolyte interface [38]. Again, we observed the lowest R_s value for the SnO_2:W 0.5% and SnO_2:W 0.7% based supercapacitors. A small semicircle in the high-frequency region is associated with the charge transfer resistance (R_{ct}), which is not visible for either device. The diameter of the overall Nyquist plot, which ranges in total frequency, can also be related to R_{ct} if the small semicircle in the high-frequency region is missing indicating low R_{ct} values for all supercapacitors, including SnO_2:W 0.5% and SnO_2:W 0.7% based ones [39].

Z-fit was performed to determine the equivalent circuit values. The fitted curve and the equivalent circuit used are shown in Figure S-Zfit⋆. Here, R_1 represents the solution resistance (R_s), R_2 is the charge transfer resistance (R_{ct}), and Q denotes a constant phase element (CPE), which is a more generalized impedance element that accounts for non-idealities in the capacitor's behavior. Q_1 in the circuit is analogous to C_{dl}, which is the double-layer capacitance, while C_2 or Q_2 represents a pseudo-capacitance (which was also discussed in the CV section). W shows the Warburg impedance from ion diffusion in the electrolyte at a low-frequency region. L is the inductance component, a negative imaginary impedance (downward curve) at higher frequencies. This feature represents an electrochemical system where unusual inductance effects may occur due to component wiring or stray current. The fitted values of the components are presented in Table 2, where a high C_{dl} and low R_s and R_{ct} values were obtained for the best performing device employing SnO_2:W 0.5% as an electrode material, as compared to all the other devices.

In W-doped SnO_2 electrodes, the electrochemical impedance data reflect two main resistive contributions: the interfacial resistance of the SnO_2 matrix and the charge-transfer resistance associated with the W^{5+}/W^{6+} redox sites. At high frequencies, the response is dominated by the intrinsic SnO_2/electrolyte interface, which governs double-layer charging and electron transport through the oxide network. At intermediate frequencies, an additional process becomes evident in the doped samples, corresponding to the kinetics of the W^{5+}/W^{6+} redox couple. These W-related redox centers provide extra pseudocapacitive storage and introduce a distinct charge-transfer resistance compared to the undoped oxide. At low frequencies, the spectra are influenced by ion diffusion within the porous electrode. W doping modifies this pathway by creating oxygen vacancies (shown in PL, Raman, and EPR results) and structural distortions that open additional ion channels and enhance electrolyte accessibility. Thus, while the undoped material shows mainly interfacial resistance linked to SnO_2, the doped systems exhibit a superimposed W-related charge-transfer process together with improved ionic transport, which explains both the higher capacitance and the altered impedance response of the 0.5% W-doped electrode.

The galvanostatic charge–discharge and capacitance retention graphs are shown in Fig. 7c and b, obtained with the GCPL technique. The capacitance retention plotted for 10 000 cycles shows the cyclic stability of the tested device. We observed that, in general, all devices showed excellent cyclic stability, with the lowest retention obtained for SnO_2:W 0.5% based device, which showed a retention of about 90% after 10 000 cycles. The best performing device with the lowest retention, this behavior is likely linked to its enhanced pseudocapacitive activity, as revealed by cyclic voltammetry and Dunn analysis, which involves redox reactions at or near the electrode surface. While these redox processes contribute significantly to the charge storage process, making the material more susceptible to structural degradation, volume fluctuations, and surface passivation over prolonged cycling.

Furthermore, the increased concentration of W dopants and associated oxygen vacancies may introduce lattice distortions or create chemically unstable sites that promote irreversible side reactions in the alkaline KOH electrolyte. Fig. 7c shows the charge–discharge curves for all devices, where the second cycle is presented. The result supports our previous observation, where higher W concentrations show the longest discharge time, with the best performing SnO_2:W 0.5% based supercapacitor device showing the best result, followed by SnO_2:W 0.7% based device. All other device shows more or less similar times, but far shorter. The charge–discharge curve for the SnO_2:W 0.5% and SnO_2:W 0.7% based device also highlights the increased influence of pseudo-capacitance for charge storage as observed in the CV results. An EDLC-type curve exhibits a perfect triangular shape with symmetry in charging and discharging; however, with pseudo-capacitance, some distortion occurs in this perfect triangle, as we observed for these two devices, where at lower voltage, the curve becomes slightly horizontal, highlighting redox activity.

The supercapacitive properties of the proposed material were also evaluated in an asymmetric SC device to get a better insight into the synergy and application possibilities. Figures S-Asym⋆ (a)–(e) shows the electrochemical measurements of one asymmetric cell, which is assembled using the best performing SnO_2:W0.5 material on one side and active carbon on the other, keeping all the other parameters the same. The results show a drop in current response (Figure S-Asym⋆ (a) and (b)) and the calculated specific capacitance from the CV data (Figure S-Asym⋆ (c)). This can be explained by the increased EDLC influence in the supercapacitor cell due to the presence of the carbon-based material. The disappearance of the redox peaks and shifting of the CV curve to a more quasi-rectangular shape highlight the reduction in pseudocapacitance. The Nyquist plot (Figure S-Asym⋆ (d)) and the charge discharge curve (Figure S-Asym⋆ (e)) also show low impedance and shorter discharge time for the asymmetric SC device. These results

Table 3
Electrochemical performance values of various SnO_2 based materials; specific capacitance (C_p), energy density (E_D) and power density (P_D)

Sample	C_p / F/g	E_D / Wh/Kg	P_D / W/Kg	Ref.
SO_4^{2-}/SnO_2	51.95	–	–	[16]
SnS_2-SnO_2	149	–	–	[40]
SnO_2 - rGO	262.2	–	–	[41]
MoS_2-SnO_2	61.6	–	–	[42]
SnO_2:Au	234	13.5	4500	[43]
SnO_2:Zr	166	–	–	[44]
SnO_2 - CC	247	–	–	[45]
SnO_2	122	–	–	[46]
SnO_2:Mn-Al	973.7	24.3	283.2	[47]
SnO_2-CuS:Y	252	16.2	740	[44]
SnO_2-ZnO	538.9	14.80	2512.35	[48]
SnO_2-MoS_2 - GO	102	32	5520	[49]
SnO_2-SnSe - AC	93.8	33.4	4003.7	[50]
SnO_2:Fe	270	–	–	[51]
SnO_2:Cu	251	–	–	[51]
SnO_2:Zn	223	–	–	[51]
$SnO_2-Co_3O_4$	606	52.2	6280	[52]
ZnO:Mn	340	47.1	59 700	[53]
MnO_2	603	50	3570	[54]
RuO_2	400	25	10 560	[55]
SnO_2:W	268	36.8	2650	t.w.

show that synergy between the Sn_2:W 0.5 electrode components in symmetric combination is more favorable to enhance the supercapacitor performance compared to the asymmetric device.

The positive impact of W-doping on the electrochemical performance of SnO_2 is evident in the results obtained by supercapacitor measurements. As shown in the EPR and XPS results, the variable valence state of W ions was crucial in achieving high specific capacitance values. The W-ions exhibit a mixed valence state of W^{5+} and W^{6+}, facilitating an enhanced faradaic reaction in the cell, resulting in high supercapacitive performance. As also shown by Li et al. [56], W^{5+}/W^{6+} redox pairs enable fast charge transfer via hopping processes between different valence states of cations at relatively low activation energies. While W-doped SnO_2 shows enhanced capacitance and improved charge storage behavior, certain limitations should also be acknowledged. First, as with most aqueous KOH-based supercapacitors, the voltage window is restricted to 1.0 V due to the thermodynamic decomposition of water. Extending the potential range beyond this limit risks electrolyte breakdown and gas evolution, which can compromise long-term stability. This constraint inherently limits the maximum energy density achievable in aqueous systems, even when electrode performance is optimized. Second, although tungsten doping effectively tunes the defect chemistry and introduces additional redox-active sites, it also adds a cost factor compared to pristine SnO_2. While the low doping levels (≤0.7%) mitigate this concern to some extent, large-scale implementation would require a careful balance between performance gains and economic feasibility.

Table 3 compares various undoped and doped SnO_2-based materials' supercapacitive properties along with SnO2 based composites and different metalic oxides [40,43–48,53–55]. It is important to note that in this study, no carbon-based booster materials were used to enhance the energy storage capability of the materials, like, for example, in the work reported by Zhang et al. [41], where SnO_2 nanorods/reduced graphene oxide nanocomposites were prepared using a two-step hydrothermal method. The specific capacitance of this composite had a maximum value of 262.2 F/g at a current density of 100 mA/g in 1 M Na_2SO_4 electrolyte. Another similar work was presented by Zhang et al. [57], where a three-dimensional lamellar SnO_2 nanostructure was grown on carbon cloth using a hydrothermal method. The specific capacitance reached 247 F/g at a current density of 1 A/g. The capacitance retention remained at approximately 76.9% after 10,000 cycles. Although these studies report slightly higher specific capacitance values, the stability of the W-doped SnO_2 material is significantly improved. Prabukumar et al. [42] reported MoS_2-SnO_2 nanocomposite materials that were used for supercapacitor applications, where SnO_2 nanoparticles were placed on the surface of MoS_2 nanosheets by a ligand exchange process. The composites had a specific capacitance value of 61.6 F/g. In a study that investigated asymmetric supercapacitors using GO as the negative electrode and SnO_2-MoS_2 composite as the positive electrode [49], the maximum reported capacitance value at a current density of 1 A/g was 102 F/g, significantly lower than the value obtained in this study (268 F/g). The energy density was also lower (32 Wh/kg). However, the power density was much higher (5520 W/kg), and the cycling stability was 92.2% after 5000 cycles compared with 80% after 2000 cycles in this study. In another study, Shah et al. [50] tested an asymmetric supercapacitor using as electrode material SnO_2-SnSe nanocomposite for the cathode and activated carbon as an anode. The specific capacitance obtained was 93.8 F/g, with energy and power densities of 33.4 Wh/kg and 4003.7 W/kg, respectively. A study by Shah et al. [52] investigated $SnO_2-Co_3O_4$ nanocomposites as an electrode material for supercapacitors, and obtained a specific capacitance of 606 F/g. Inspired by this remarkable performance, the same study realized an asymmetric supercapacitor device, using $SnO_2-Co_3O_4$ nanocomposite for the cathode material and activated carbon for the anode material. The specific capacitance was 116 F/g, energy density 52.2 Wh/kg, and power density 6280 W/kg. Some studies report on transitional metal-doped SnO_2 materials used for supercapacitor applications that present good results for the specific capacitance value. Researchers examining SnO_2 doped with transition metals Fe, Cu, and Zn found that at a current density of 0.5 A/g, the specific capacitances were 270, 251, and 223 F/g, respectively [51]. It was observed that the specific capacitance declined markedly at increased current densities. The study, which was conducted in a 3-electrode configuration, suggested that these capacitance values would likely decrease in practical testing devices. In comparison, our research demonstrated a superior specific capacitance of 268 F/g with the best-performing SnO_2:W 0.5-based SC device, highlighted by improved energy and power density over W-doped SnO_2. Literature shows a broad range of specific capacitance values for SnO_2-based electrode materials in supercapacitor applications, highly influenced by testing conditions and the choice between a 2- or 3-electrode setup, affecting their overall performance considerably. This study evaluates the complete supercapacitor device without carbon-based materials, showcasing the potential of W-doped SnO_2 as electrodes. Moreover, precise defect engineering, through optimal synthesis and thorough defect analysis using advanced techniques like EPR, XPS and PL, is crucial for enhancing supercapacitor performance.

4. Conclusions

In summary, introducing W^{5+}/W^{6+} redox pairs into the SnO_2 structure enables fast charge transfer via hopping processes between different valence state cations at a relatively lower activation energy, thereby enhancing the supercapacitive properties of the host material. Adding 0.5% tungsten to SnO_2 improves the specific capacitance almost three times, increasing it to 268 F/g at a 2 mV/s scan rate, with remarkable energy and power densities of 36.8 Wh/kg and 2650 W/kg, respectively. The presence of the W^{5+}/W^{6+} redox pairs was evidenced by electron paramagnetic resonance and X-ray photoelectron spectroscopy. Additionally, Raman and photoluminescence spectroscopy proved the existence of oxygen vacancies in the undoped SnO_2, key factors in forming the pairs mentioned above. SnO_2:W 0.5% shows prominent variations in the supercapacitive features, with the charge-storage process dominated by pseudo-capacitance. The drop in the peak current values at a lower scan rate relates to the rate capability of the device, which presents great capacitance retention values after 2000 cycles of 80%, which proves that W^{5+}/W^{6+} redox pairs play a crucial role in enhancing the supercapacitive properties of metal oxides, especially for SnO_2.

CRediT authorship contribution statement

Karlo Maskaric: Writing – original draft, Visualization, Investigation, Formal analysis. **Ana Varadi:** Formal analysis. **Ameen Uddin Ammar:** Writing – original draft, Investigation, Formal analysis. **Adriana Popa:** Writing – original draft, Investigation, Formal analysis. **Dana Toloman:** Writing – original draft, Investigation, Formal analysis. **Sergiu Macavei:** Investigation, Formal analysis. **Lucian Barbu Tudoran:** Formal analysis. **Cristian Leostean:** Writing – original draft, Investigation, Formal analysis. **Emre Erdem:** Writing – original draft, Supervision, Investigation, Formal analysis. **Maria Stefan:** Writing – original draft, Supervision, Investigation, Formal analysis. **Arpad Mihai Rostas:** Writing – original draft, Visualization, Validation, Supervision, Investigation, Formal analysis, Conceptualization.

Declaration of competing interest

The authors declare that they have no known competing financial interests or personal relationships that could have appeared to influence the work reported in this paper.

Acknowledgments

The authors would like to express appreciation for the financial support of the Ministry of Research, Innovation and Digitalization, Romania's National Recovery and Resilience Plan, PNRR-III-C9-2022-I8, CF 163/15.11.22, financing contract no. 760097/23.05.23.

Appendix A. Supplementary data

Supplementary material related to this article can be found online at https://doi.org/10.1016/j.electacta.2025.147515.

Data availability

Data will be made available on request.

References

[1] V.S. Arutyunov, G.V. Lisichkin, Energy resources of the 21st century: Problems and forecasts. Can renewable energy sources replace fossil fuels, Russ. Chem. Rev. 86 (8) (2017) 777.
[2] D. Maradin, Advantages and disadvantages of renewable energy sources utilization, Int. J. Energy Econ. Policy 11 (3) (2021) 176–183.
[3] S. Liu, L. Wei, H. Wang, Review on reliability of supercapacitors in energy storage applications, Appl. Energy 278 (2020) 115436.
[4] M.E. Şahin, F. Blaabjerg, A. Sangwongwanich, A comprehensive review on supercapacitor applications and developments, Energies 15 (3) (2022) 674.
[5] A. Shukla, S. Sampath, K. Vijayamohanan, Electrochemical supercapacitors: Energy storage beyond batteries, Current Sci. 79 (12) (2000) 1656–1661.
[6] N.I. Jalal, R.I. Ibrahim, M.K. Oudah, A review on supercapacitors: Types and components, J. Phys. Conf. Ser. 1973 (1) (2021) 012015.
[7] J. Libich, J. Máca, J. Vondrák, O. Čech, M. Sedlaříková, Supercapacitors: Properties and applications, J. Energy Storage 17 (2018) 224–227.
[8] Y. Wu, C. Cao, The way to improve the energy density of supercapacitors: Progress and perspective, Sci. China Mater. 61 (12) (2018) 1517–1526.
[9] A.U. Ammar, I.D. Yildirim, F. Bakan, E. Erdem, ZnO and MXenes as electrode materials for supercapacitor devices, Beilstein J. Nanotechnol. 12 (1) (2021) 49–57.
[10] K. Makgopa, A. Bello, K. Raju, K.D. Modibane, M.J. Hato, Nanostructured metal oxides for supercapacitor applications, Emerg. Nanostructured Mater. Energy Environ. Sci. (2019) 247–303.
[11] I. Shaheen, I. Hussain, T. Zahra, M.S. Javed, S.S.A. Shah, K. Khan, M.B. Hanif, M.A. Assiri, Z. Said, W.U. Arifeen, et al., Recent advancements in metal oxides for energy storage materials: Design, classification, and electrodes configuration of supercapacitor, J. Energy Storage 72 (2023) 108719.
[12] T.K. Shivasharma, R. Sahu, M. Rath, S.J. Keny, B.R. Sankapal, Exploring tin oxide based materials: A critical review on synthesis, characterizations and supercapacitive energy storage, Chem. Eng. J. (2023) 147191.
[13] R. Ahmed, G. Nabi, N. Khalid, F. Ali, M. Tanveer, Controlled synthesis and enhanced electrochemical performance of tungsten doped NiO nano-sheets for supercapacitors, Appl. Nanosci. 11 (2021) 1279–1289.
[14] X. Huo, S. Jiang, P. Liu, M. Shen, S. Qiu, M.-Y. Li, Molybdenum and tungsten doped SnO_2 transparent conductive thin films with broadband high transmittance between the visible and near-infrared regions, CrystEngComm 19 (30) (2017) 4413–4423.
[15] G.K. Dalapati, H. Sharma, A. Guchhait, N. Chakrabarty, P. Bamola, Q. Liu, G. Saianand, A.M.S. Krishna, S. Mukhopadhyay, A. Dey, et al., Tin oxide for optoelectronic, photovoltaic and energy storage devices: A review, J. Mater. Chem. A 9 (31) (2021) 16621–16684.
[16] Y. Gao, J. Wu, W. Zhang, Y. Tan, T. Tang, S. Wang, B. Tang, J. Zhao, SO_{42}-/SnO_2 as a new electrode for electrochemical supercapacitors, Ceram. Int. 40 (6) (2014) 8925–8929.
[17] B. Varshney, M. Siddiqui, A.H. Anwer, M.Z. Khan, F. Ahmed, A. Aljaafari, H.H. Hammud, A. Azam, Synthesis of mesoporous SnO_2/NiO nanocomposite using modified sol–gel method and its electrochemical performance as electrode material for supercapacitors, Sci. Rep. 10 (1) (2020) 11032.
[18] U. Nithiyanantham, A. Ramadoss, S. Kundu, Synthesis and characterization of DNA fenced, self-assembled SnO_2 nano-assemblies for supercapacitor applications, Dalton Trans. 45 (8) (2016) 3506–3521.
[19] D. Toloman, A. Popa, M. Stefan, T.D. Silipas, R.C. Suciu, L. Barbu-Tudoran, O. Pana, Enhanced photocatalytic activity of Co doped SnO_2 nanoparticles by controlling the oxygen vacancy states, Opt. Mater. 110 (2020) 110472.
[20] M. Stefan, C. Leostean, O. Pana, A. Popa, D. Toloman, S. Macavei, I. Perhaita, L. Barbu-Tudoran, D. Silipas, Interface tailoring of SnO_2-TiO_2 photocatalysts modified with anionic/cationic surfactants, J. Mater. Sci. 55 (8) (2020) 3279–3298.
[21] P. Senthilkumar, S. Raja, R.R. Babu, G. Vasuki, Enhanced electrical and optoelectronic properties of W doped SnO_2 thin films, Opt. Mater. 126 (2022) 112234.
[22] D.S. Aidhy, B. Liu, Y. Zhang, W.J. Weber, Chemical expansion affected oxygen vacancy stability in different oxide structures from first principles calculations, Comput. Mater. Sci. 99 (2015) 298–305.
[23] L. Liu, T. Li, X. Wu, J. Shen, P. Chu, Identification of oxygen vacancy types from Raman spectra of SnO nanocrystals, J. Raman Spectrosc. 43 (10) (2012) 1423–1426.
[24] I. Ullah, A. Munir, S. Muhammad, S. Ali, N. Khalid, M. Zubair, M. Sirajuddin, S.Z. Hussain, S. Ahmed, Y. Khan, et al., Influence of W-doping on the optical and electrical properties of SnO_2 towards photocatalytic detoxification and electrocatalytic water splitting, J. Alloys Compd. 827 (2020) 154247.
[25] C. Bigey, L. Hilaire, G. Maire, Catalysis on Pd/WO_3 and Pd/WO_2: Effect of the modifications of the surface states due to redox treatments on the skeletal rearrangement of hydrocarbons: Part I. physical and chemical characterizations of catalysts by BET, TPR, XRD, XAS, and XPS, J. Catalysis 184 (2) (1999) 406–420.
[26] A. Sadeghzadeh-Attar, Enhanced photocatalytic hydrogen evolution by novel Nb-doped SnO_2/V_2O_5 heteronanostructures under visible light with simultaneous basic red 46 dye degradation, J. Asian Ceram. Soc. 8 (3) (2020) 662–676.
[27] R. Mishra, A. Kushwaha, P.P. Sahay, Influence of Cu doping on the structural, photoluminescence and formaldehyde sensing properties of SnO_2 nanoparticles, RSC Adv. 4 (8) (2014) 3904–3912.
[28] A. Sadeghzadeh-Attar, I. Akhavan-Safaei, M.R. Bafandeh, UV-visible absorption and photoluminescence characteristics of SnO_2 nano-tube/wire arrays fabricated by LPD method, Int. J. Appl. Ceram. Technol. 15 (5) (2018) 1084–1094.
[29] Y. Hajimoto, E. Yamaka, M. Nagasawa, S. Shionoya, Electron spin resonance in reduced SnO_2, Phys. Lett. 23 (1) (1966) 50–51.
[30] M. Itoh, H. Hattori, K. Tanabe, Catalytic sites on SnO_2 and TiO_2&SnO_2 for the isomerization of 1-butene, J. Catalysis 43 (1–3) (1976) 192–199.
[31] A. Silva, F. Hurdley, A.L.M. de Oliveira, T. Slater, A. da Silva Maia, A. Folli, I.M.G. dos Santos, An EPR investigation on reduced Sn centres in $SrSnO_3$ perovskite, Mater. Lett. 368 (2024) 136705.
[32] S. Maniv, W. Low, A. Gabay, EPR spectrum of W^{5+} in single crystals of Cs_2ZrCl_6 and Cs_2HfCl_6, J. Phys. Chem. Solids 32 (4) (1971) 815–817.
[33] H. Mollet, B. Gerstein, An EPR study of W^{5+} in a recently discovered triclinic tungsten bronze, $Na_{0.33}WO_3$, J. Chem. Phys. 60 (4) (1974) 1440–1446.
[34] R.R. Rakhimov, D.E. Jones, H.L. Rocha, A.I. Prokof'ev, A.I. Aleksandrov, Electron paramagnetic resonance study of W^{5+} pairs in Lithium- Tungsten phosphate glasses, J. Phys. Chem. B 104 (47) (2000) 10973–10977.
[35] J.P.A. dos Santos, F.C. Rufino, J.I.Y. Ota, R.C. Fernandes, R. Vicentini, C.J. Pagan, L.M. Da Silva, H. Zanin, Best practices for electrochemical characterization of supercapacitors, J. Energy Chem. 80 (2023) 265–283.
[36] W.K. Chee, H.N. Lim, I. Harrison, K.F. Chong, Z. Zainal, C.H. Ng, N.M. Huang, Performance of flexible and binderless polypyrrole/graphene oxide/zinc oxide supercapacitor electrode in a symmetrical two-electrode configuration, Electrochim. Acta 157 (2015) 88–94.
[37] R. Raavi, S. Archana, P.A. Reddy, P. Elumalai, Performances of dual carbon multi-ion supercapacitors in aqueous and non-aqueous electrolytes, Energy Adv. 2 (3) (2023) 385–397.
[38] P. Widiatmoko, N. Nugraha, H. Devianto, I. Nurdin, T. Prakoso, Upscaled synthesis of carbon nanotube from palm oil mill effluent using pyrolysis for supercapacitor application, IOP Conf. Ser. Mater. Sci. Eng. 823 (2020) 012040.

[39] A.C. Lazanas, M.I. Prodromidis, Electrochemical impedance spectroscopy - a tutorial, ACS Meas. Sci. Au 3 (3) (2023) 162–193.
[40] P. Asen, M. Haghighi, S. Shahrokhian, N. Taghavinia, One step synthesis of SnS_2-SnO_2 nano-heterostructured as an electrode material for supercapacitor applications, J. Alloys Compd. 782 (2019) 38–50.
[41] Y. Zhang, M. Liu, S. Sun, L. Yang, The preparation and characterization of SnO_2/rGO nanocomposites electrode materials for supercapacitor, Adv. Compos. Lett. 29 (2020) 2633366X20909839.
[42] C. Prabukumar, M.M.J. Sadiq, D.K. Bhat, K.U. Bhat, SnO_2 nanoparticles functionalized MoS_2 nanosheets as the electrode material for supercapacitor applications, Mater. Res. Express 6 (8) (2019) 085526.
[43] S. Anshu, S. Priya, D. Mandal, R. Rahul, T. Singh, A. Chandra, 2D flakes of Au decorated SnO_2 nanoparticles as electrode material for high performing supercapacitor, J. Phys. D: Appl. Phys. 56 (20) (2023) 205501.
[44] S. Asaithambi, P. Sakthivel, M. Karuppaiah, K. Balamurugan, R. Yuvakkumar, M. Thambidurai, G. Ravi, Synthesis and characterization of various transition metals doped SnO_2@MoS_2 composites for supercapacitor and photocatalytic applications, J. Alloys Compd. 853 (2021) 157060.
[45] J. Zhang, Y. Sun, J. Xu, Fabrication of antimony doped tin oxide nanopowders as an advanced electrode material for supercapacitors, Micro Nano Lett. 14 (3) (2019) 254–258.
[46] K. Manikandan, S. Dhanuskodi, N. Maheswari, G. Muralidharan, SnO_2 nanoparticles for supercapacitor application, Dae Solid State Phys. Symp. 2015 1731 (1) (2016) 050048.
[47] A. Sohail, M. Aalim, R. Ahmad, U. Altaf, M. Shah, K. Majid, Enhanced electrochemical characteristics of Mn-Al-co-doped SnO nanostructures for high-performance supercapacitor application, J. Mater. Sci., Mater. Electron. 35 (19) (2024) 1302.
[48] N.S. Lopa, M.K. Akbari, D. Wu, F. Verpoort, S. Zhuiykov, Two-dimensional SnO_2-ZnO nanohybrid electrode fabricated via atomic layer deposition for electrochemical supercapacitors, Energy Fuels 37 (4) (2023) 3142–3151.
[49] K. Rafique, N. Hassan, M.Z.U. Shah, S.I. Al-Saeedi, A. Shah, M.S.U. Shah, U. Aziz, M. Sajjad, A.A. Alanazi, H.M. Hassan, Improved performance in asymmetric supercapacitors using SnO_2–MoS_2 composite microspheres, Surfaces Interfaces 44 (2024) 103650.
[50] M.Z.U. Shah, J. Shah, K. Hayat, S. Shah, I. Hussain, A.U. Khan, M.S. Shah, H. Hou, M. Sajjad, S.I. Al-Saeedi, et al., Optimizing performance: achieving high capacitance and cycling durability in alkaline electrolyte with SnO_2/SnSe - AC/KOH-based aqueous hybrid supercapacitor, J. Energy Storage 75 (2024) 109662.
[51] S. Asaithambi, P. Sakthivel, M. Karuppaiah, G.U. Sankar, K. Balamurugan, R. Yuvakkumar, M. Thambidurai, G. Ravi, Investigation of electrochemical properties of various transition metals doped SnO2 spherical nanostructures for supercapacitor applications, J. Energy Storage 31 (2020) 101530.
[52] M.Z.U. Shah, J. Feng, A. Shah, M. Sajjad, V. Tirth, M.S. Shah, Wet-chemical synthesis of SnO2-Co3O4 microflower electrode for high energy density in aqueous asymmetric supercapacitors, J. Energy Storage 108 (2025) 115081.
[53] M.H. Aleinawi, A.U. Ammar, D. Şentürk, L. Barbu-Tudoran, O.J. Ajala, D. Eşkin, F.B. Misirlioglu, A.M. Rostas, E. Erdem, Microwave-tuned mn-doped ZnO for all-in-one supercapacitors: Correlating defect chemistry with electrochemical behavior, J. Colloid Interface Sci. (2025) 138012.
[54] Z. Yu, B. Duong, D. Abbitt, J. Thomas, Highly ordered MnO2 nanopillars for enhanced supercapacitor performance, Adv. Mater. 25 (24) (2013) 3302–3306.
[55] F. Yu, L. Pang, H.-X. Wang, Preparation of mulberry-like RuO2 electrode material for supercapacitors, Rare Met. 40 (2) (2021) 440–447.
[56] M. Li, Y. Xiong, X. Liu, X. Bo, Y. Zhang, C. Han, L. Guo, Facile synthesis of electrospun MFe_2O_4 (M=Co, Ni, Cu, Mn) spinel nanofibers with excellent electrocatalytic properties for oxygen evolution and hydrogen peroxide reduction, Nanoscale 7 (19) (2015) 8920–8930.
[57] Y. Zhang, Z. Hu, Y. Liang, Y. Yang, N. An, Z. Li, H. Wu, Growth of 3D SnO_2 nanosheets on carbon cloth as a binder-free electrode for supercapacitors, J. Mater. Chem. A 3 (29) (2015) 15057–15067.